A dynamic model-based approach to motion and deformation tracking of prosthetic valves from biplane x-ray images

Martin G. Wagner
Department of Medical Physics, University of Wisconsin-Madison, Madison, WI, USA
Department of Radiology, University of Wisconsin-Madison, Madison, WI, USA

Charles R. Hatt, David A. P. Dunkerley, and Lindsay E. Bodart
Department of Medical Physics, University of Wisconsin-Madison, Madison, WI, USA

Amish N. Raval
Department of Medicine, University of Wisconsin-Madison, Madison, WI, USA

Michael A. Speidel[a)]
Department of Medical Physics, University of Wisconsin-Madison, Madison, WI, USA
Department of Medicine, University of Wisconsin-Madison, Madison, WI, USA

(Received 23 May 2017; revised 2 April 2018; accepted for publication 2 April 2018; published 3 May 2018)

Purpose: Transcatheter aortic valve replacement (TAVR) is a minimally invasive procedure in which a prosthetic heart valve is placed and expanded within a defective aortic valve. The device placement is commonly performed using two-dimensional (2D) fluoroscopic imaging. Within this work, we propose a novel technique to track the motion and deformation of the prosthetic valve in three dimensions based on biplane fluoroscopic image sequences.
Methods: The tracking approach uses a parameterized point cloud model of the valve stent which can undergo rigid three-dimensional (3D) transformation and different modes of expansion. Rigid elements of the model are individually rotated and translated in three dimensions to approximate the motions of the stent. Tracking is performed using an iterative 2D–3D registration procedure which estimates the model parameters by minimizing the mean-squared image values at the positions of the forward-projected model points. Additionally, an initialization technique is proposed, which locates clusters of salient features to determine the initial position and orientation of the model.
Results: The proposed algorithms were evaluated based on simulations using a digital 4D CT phantom as well as experimentally acquired images of a prosthetic valve inside a chest phantom with anatomical background features. The target registration error was 0.12 ± 0.04 mm in the simulations and 0.64 ± 0.09 mm in the experimental data.
Conclusions: The proposed algorithm could be used to generate 3D visualization of the prosthetic valve from two projections. In combination with soft-tissue sensitive-imaging techniques like transesophageal echocardiography, this technique could enable 3D image guidance during TAVR procedures. [https://doi.org/10.1002/mp.12913]

Key words: fluoroscopy, image visualization, registration, tracking

1. INTRODUCTION

Transcatheter valve replacement and repair have recently emerged as a minimally invasive alternative to surgery for aortic, mitral, pulmonic, and tricuspid valvular heart disease. For example, the United States Food and Drug Administration has approved transcatheter aortic valve replacement (TAVR) for the treatment of severe aortic valve stenosis in patients who are considered to be at intermediate or high risk with surgical aortic valve replacement. Currently, approved TAVR devices are either balloon expandable (Sapien XT and S3, Edwards Lifesciences, Irvine, CA, USA) or self-expanding (CoreValve and CoreValve Evolut R, Medtronic, Minneapolis, MN, USA), although the balloon expandable variety was first to market and is most widely used worldwide.[1] In this procedure, a stent-supported valve is mounted on an expandable balloon and carefully positioned within the native aortic valve annulus. The aortic valve annular plane is typically defined by the preoperative CT scan and then confirmed using intraoperative C-arm aortography. The balloon is then inflated to deploy the stent valve and then deflated. During the initial portion of the deployment, minor adjustments can be made to improve the position of the stent valve. Major complications such as perivalvular regurgitation, valve embolization, and coronary artery obstruction occur if the valve is deployed too low or too high relative to the aortic valve annular plane. Imaging methods that enhance device visualization with respect to the local anatomy may improve procedure success and prevent these complications.

In addition to fluoroscopic guidance, ultrasound imaging such as transesophageal echocardiography (TEE) can be used to provide three-dimensional (3D) soft-tissue information in real time. Echocardiography/x-ray fusion techniques have been proposed to combine the soft-tissue information

provided by the TEE with a two-dimensional (2D) fluoroscopic display.[2–6] In these techniques, the transformation between the coordinate systems of the imaging modalities has to be known. Since the ultrasound coordinate system is dependent on the position and orientation of the probe, real-time tracking of the probe is required. In Ref. [2–4], the transformation was estimated for each frame by iteratively forward projecting a 3D model of the ultrasound probe and minimizing the difference between the virtual projection and the fluoroscopy image. The approach proposed in Lang et al.[5] uses external fiducials attached to the probe and a Procrustes analysis to register the probe position to the fluoroscopic images. Recent display approaches have been to render the semitransparent 3D echo surface onto the 2D x ray.[6] Although the x-ray image provides the high spatial and temporal resolution needed for device visualization, and the echo imaging provides good soft-tissue visualization, the display remains in a 2D projection format. A more intuitive feel for the relationship between prosthetic valve and anatomy might be obtained by remaining in a 3D view. However, this requires 3D representation of the device itself, as the geometry of the expanding prosthetic valve is not easy to visualize in ultrasound (see Fig. 1). Therefore, the purpose of this work is to propose a novel technique to generate a time-resolved 3D representation of a prosthetic valve from biplane fluoroscopic image sequences.

Many techniques for the 3D reconstruction of objects from biplane fluoroscopic images have been investigated. However, the approaches vary depending on the type of object being reconstructed. In the simplest case, if a single 2D point is given in each image plane, its 3D position can be determined by triangulation. An evaluation of the 3D point reconstruction accuracy for known-point correspondences showed that an error of less than 1 mm is possible depending on the angulation of the C-arms.[7] In most practical applications, the point correspondences are not implicitly known. However, in many cases, it is possible to solve this problem using a priori knowledge of the object. One example is the reconstruction of curvilinear devices such as guidewires. By segmenting and connecting the 2D device path in each image plane, corresponding pairs of points along the 3D path can be extracted.[8–10] Similar approaches can be used to reconstruct 3D vessel trees from biplane images. For example, Wahle et al.[11] use manually selected nodes to extract and reconstruct 3D vessel centerlines from biplane angiograms. Other approaches iteratively manipulate a 3D model of the object of interest until a similarity measure between a projection of the object and the 2D images is optimized. This was investigated for catheters using a 3D B-spline curve as model.[12] The *deformable known-component registration* proposed in Ref. [13] uses a B-spline model to estimate the position, orientation, and shape of K-wires and spinal fixation rods from two to three x-ray images acquired with different gantry angles. In Ref. [14,15], techniques for the 3D localization of ablation catheters with multiple radio-opaque electrodes near the tip are described, where the model describes the number and distance between the electrodes as well as their individual shapes. Model-based vasculature reconstruction techniques based on snakes were proposed in Ref. [16,17], where the shape and position of the snakes are defined by a function of internal and external energies. The internal energy preserves the smoothness of the curve, while the external energy is a function of the acquired image data. A binary reconstruction approach for heart chambers was investigated in Prause et al.[18], where a priori knowledge is included by assuming similarity between adjacent frames. Statistical shape models have also been used for the reconstruction of 3D shapes from biplane images.[19–23] This requires a training dataset, where each training surface is labeled and mapped into a common domain. The model is then determined by the average shape and the principal components.

The present work proposes a 3D tracking framework for a class of dynamic devices, which expand and change shape while being deployed. Recovering the shape and position of an object from only two views is generally an underdetermined problem. However, by using prior knowledge about

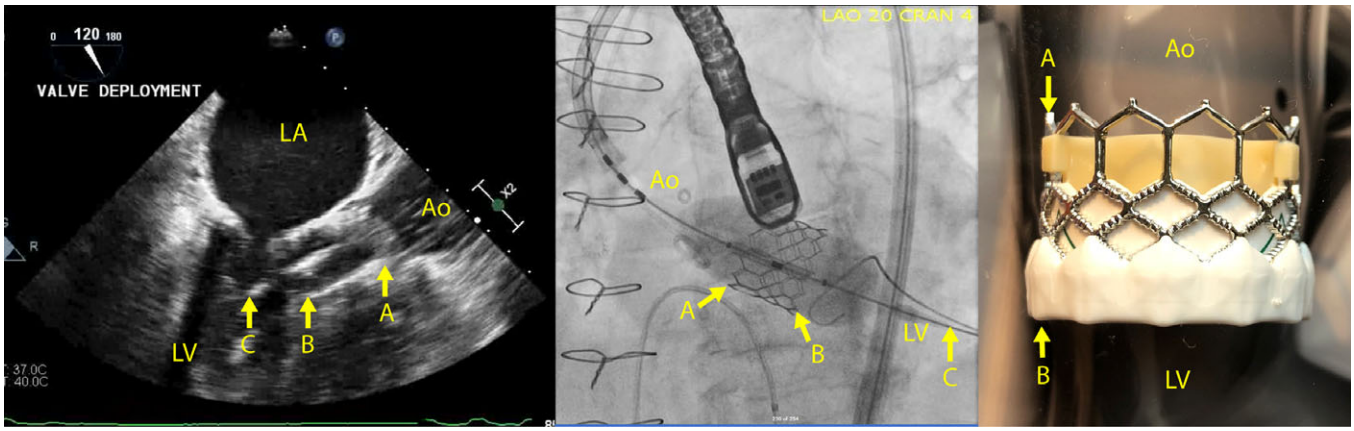

FIG. 1. Ultrasound (left) and x-ray (middle) images of a fully deployed valve during a TAVR procedure. A photograph of the valve (SAPIEN 3, Edwards Lifesciences Corporation, Irvine CA, USA) is shown to the right. Anatomical regions are annotated as left atrium (LA), left ventricle (LV), and Aorta (Ao). The top of the valve frame (A), bottom of the valve frame (B), and guidewire (C) are also indicated. The stent structure of the prosthetic valve is easily visualized in the x-ray image. [Color figure can be viewed at wileyonlinelibrary.com]

the device shape and parameterizing possible deformations, the complexity of the reconstruction task can be reduced. The feasibility of this approach was previously investigated using simulations and a simple phantom study.[24] The tracking method uses the Nelder–Mead simplex algorithm[25] to optimize the parameters determining the position and shape of a point cloud model of an expanding valve stent. The model is forward projected into the 2D image space of the fluoroscopic images and the gray values for all projected model points are interpolated to determine the accuracy of the current estimate. Within this work, we present an extension of this approach, which includes preprocessing of the image data to reduce the influence of anatomical background, a more sophisticated device model that allows for a wider range of deformations, and a modified regularization term to improve the reliability of the algorithm. Additionally, an initialization technique based on FAST corner points[26] is presented. The approach is evaluated using simulated as well as experimental image data, which includes realistic anatomical background.

2. MATERIALS AND METHODS

2.A. Dynamic model

To track both motion and deformation of a prosthetic heart valve, a parameterized point cloud model representing the 3D structure of the expandable stent structure of the valve is created. The model in this work is based on a SAPIEN XT transcatheter aortic valve (26 mm, Edwards Lifesciences Corporation), as shown in Fig. 2. The device consists of a bovine pericardial tissue prosthetic valve sewn to a balloon-expandable metal stent. The technique presented here can be used for other valves of similar design.

FIG. 2. Photograph of the transcatheter heart valve (SAPIEN XT 26 mm, Edwards Lifesciences Corporation). Expandable stent structure (silver) secures the valve in place and defines the shape of the valve. Its radio-opaque structures can be used to track the valve in fluoroscopic images. [Color figure can be viewed at wileyonlinelibrary.com]

The deformable model $\boldsymbol{M}$ is created from rigid elements, where each element $\boldsymbol{E} = [\boldsymbol{p}_1 \boldsymbol{p}_2 \cdots]$ is represented by a cloud of 3D points, $\boldsymbol{p}_j = [x_j\ y_j\ z_j]^T$. The points are aligned on a rectangular grid with an isotropic grid spacing of 0.2 mm. Five different types of elements are created: vertical struts, diagonal struts, inner and outer connection points, and stent–valve connection (SVC) components. The SVC components provide the main connection to the actual prosthetic valve. The first four element types are created by a single cylindrical shape, whereas the SVC component is a combination of multiple cylinders and cuboids. A list of all element types along with the respective measurements is shown in Table I. Since the elements are rigid, the point clouds only have to be generated once.

In its default nonexpanded state, the model is the concatenation of the point–cloud matrices representing the individual elements: $\boldsymbol{M} = [\boldsymbol{E}_1\ \boldsymbol{E}_2 \cdots \boldsymbol{E}_n]$. Each element $\boldsymbol{E}_i$ can be rotated and translated within the stent structure using a rotation matrix $\boldsymbol{R}_i$ and a translation vector $\boldsymbol{t}_i$, which are in turn dependent on a set of valve shape parameters $\boldsymbol{\varphi}_e$. Therefore, the parameterized model $\boldsymbol{M}^*$ at some state of expansion can be described by the concatenation of transformed elements $\boldsymbol{E}_i^*$,

$$\boldsymbol{M}^*(\boldsymbol{\varphi}_\mathbf{e}) = [\boldsymbol{E}_1^*\ \boldsymbol{E}_2^* \cdots\ \boldsymbol{E}_n^*] \tag{1}$$

where

$$\boldsymbol{E}_i^* = \boldsymbol{R}_i(\boldsymbol{\varphi}_e)\boldsymbol{E}_i + \boldsymbol{t}_i(\boldsymbol{\varphi}_e) \tag{2}$$

and $n = 93$ elements (see Table I). The vector of valve shape parameters $\boldsymbol{\varphi}_e = [d\ s\ f_u\ f_l]$ contains the diameter d at the center of the valve, the slant s which is the ratio between the diameters at the top and the bottom of the valve, and two angles f_u and f_l describing the flare at the upper and lower end of the valve, respectively. An overview of all possible modes of expansion included in the model is shown in Fig. 3. A global rotation and translation are applied to $\boldsymbol{M}^*$ to calculate the final 3D point cloud model

$$\boldsymbol{M}(\boldsymbol{\varphi}) = \boldsymbol{R}(\boldsymbol{r})\boldsymbol{M}^*(\boldsymbol{\varphi}_e) + \boldsymbol{t}, \tag{3}$$

where $\boldsymbol{R}(\boldsymbol{r})$ is a 3D rotation matrix defined by the Euler angles $\boldsymbol{r} = [\alpha\ \beta\ \gamma]$, and $\boldsymbol{t} = [\Delta x\ \Delta y\ \Delta z]^T$ is the translation in 3D. The final model is, therefore, described by ten adjustable parameters,

TABLE I. List of all model elements with measurements. Connection points are placed at the joints between two or more vertical or diagonal struts. The stent–valve connection (SVC) component represents the connection between the stent and the actual prosthetic valve. The radius of the SVC component denotes the height and width (at the widest point) of the part.

Description	Length (mm)	Radius (mm)	Count
Connection (small)	0.4	0.4	24
Connection (big)	0.4	0.6	6
Vertical strut	8.3	0.4	6
Diagonal strut	5.7	0.4	54
SVC component	13.4	0.4 × 1.8	3

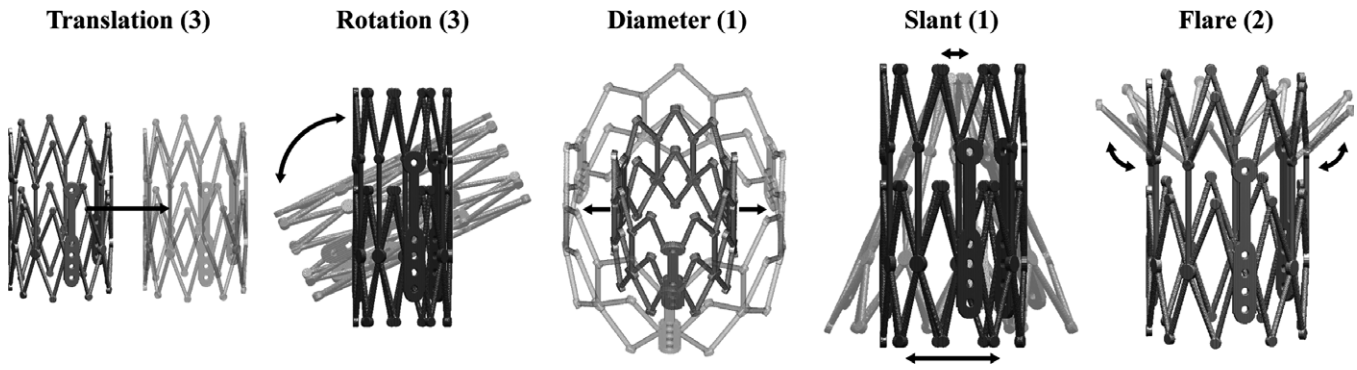

FIG. 3. Transformation parameters of the valve model. The entire model can be translated and rotated with six degrees of freedom. Additionally, the valve diameter, slant, and flare can change. Slant can occur toward the top or bottom of the stent and flare can occur on either end of the stent. The number next to the label denotes the degrees of freedom for each type of transformation.

representing six degrees of freedom for global rotation and translation and four parameters for the valve shape.

$$\boldsymbol{\varphi} = [\alpha\, \beta\, \gamma\, \Delta x\, \Delta y\, \Delta z\, d\, s\, f_u\, f_l] \tag{4}$$

2.B. Tracking algorithm

An overview of the proposed tracking algorithm is shown in Fig. 4. Two simultaneous fluoroscopic image sequences are acquired using a biplane angiography system. The images are preprocessed to enhance features corresponding to the stent of the valve. The algorithm then estimates the 3D position, orientation, and deformation of the prosthetic valve using a parameterized point cloud model. To determine the parameters that best represent the true valve position, a cost function is iteratively minimized using the Nelder–Mead method.[25] The cost for a given set of parameters $\boldsymbol{\varphi}$ is calculated by projecting the model points into the 2D image space and calculating the mean-squared value of the preprocessed images at those projected points.

2.B.1. Prerequisites

The proposed algorithm requires a biplane angiography system which acquires two simultaneous fluoroscopic image streams while the valve is deployed. Preferably, the two C-arm gantries are positioned orthogonal to each other to improve the accuracy of the 3D representation.[7] Within this work, gantry angles of −90°/0° and −45°/45° are investigated for plane A and B, respectively, where a gantry angle of 0° corresponds to an anterior–posterior and −90° to a lateral view. A calibration step has to be performed for each gantry position to estimate the 3D–2D projection matrices. Cone-beam CT calibration has been investigated previously[27–29] and therefore is not discussed further here.

2.B.2. Preprocessing

The purpose of the preprocessing step is to enhance image features which correspond to the stent structure of the prosthetic valve. Since the metal stent is highly attenuating, the projection images may be used directly for the optimization step without preprocessing. That is, a low mean-squared image value at the projected model points in both images indicates that the projected model is well aligned with the actual dark features of the device in the x-ray images, and optimization can be based on minimization of this quantity. However, preprocessing can help distinguish between the metal ridges of the stent and other highly absorbing material, such as bones, and reduce the

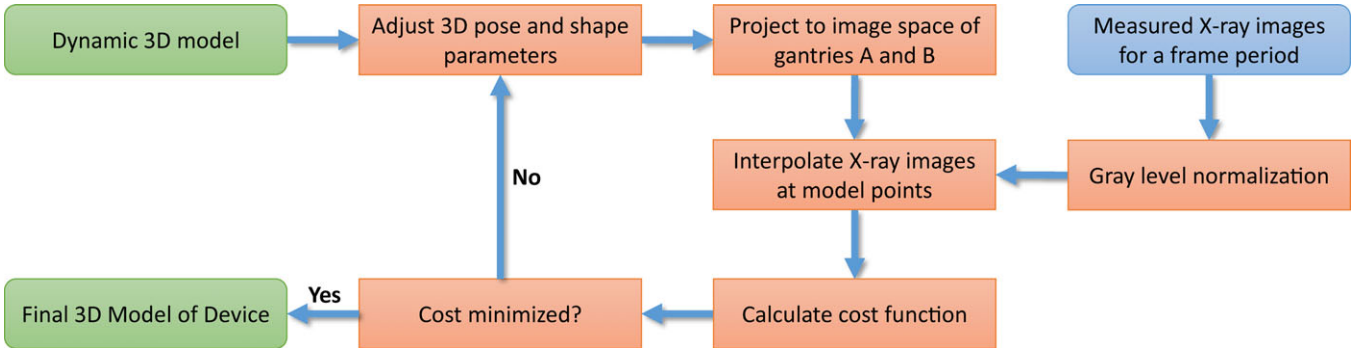

FIG. 4. Flow diagram of the proposed tracking algorithm. The initial guess of the dynamic 3D model is optimized by minimizing a cost function which is based on the gray levels in the normalized and feature-enhanced x-ray images at the positions of the forward projected points of the model. [Color figure can be viewed at wileyonlinelibrary.com]

influence of low frequency background intensity variations on the optimization procedure. Therefore, the original fluoroscopic images are converted to line integral images using software provided by the manufacturer of the imaging system. Low-frequency components are then removed from the line integral image I_L by subtracting a Gaussian-filtered version of the image

$$I_N = I_L - h_\sigma * I_L \tag{5}$$

where h_σ represents a discrete 2D Gaussian kernel with standard deviation $\sigma = 9$ pixels. To further improve the convergence properties of the optimization algorithm, Gaussian blurring with standard deviation $\sigma_o = 2.5$ pixels is applied to the normalized images I_N. The parameters were chosen empirically. A relatively large value is required for σ to filter out high frequencies generated by the valve stent. The value chosen for σ_o is dependent on the expected valve motion between adjacent frames.

2.B.3. Optimization

To calculate the cost function for a given set of parameters $\boldsymbol{\varphi}$, the 3D point cloud model is projected into the image space of both plane A and B. The respective images are then interpolated at each projected point and the squared value is calculated. Since the stent material is highly attenuating and the images are converted into line integrals in preprocessing, larger values are obtained when the model is well aligned with the true device image. Correspondingly, one may maximize the sum of the squared image values from both planes or minimize the negative sum of the squared values. Given a parameter set $\boldsymbol{\varphi}$, a cost function to be minimized was defined as

$$c(\boldsymbol{\varphi}) = -\frac{1}{2}\sum_{\forall j\in\{A,B\}}\sum_{\forall i} I_{N,j}(\boldsymbol{P}_j\boldsymbol{M}(\boldsymbol{\varphi})_i)^2 + \lambda\|\boldsymbol{\varphi}-\boldsymbol{\varphi}_o\|^2 \tag{6}$$

where $I_{N,j}$ is the preprocessed image frame of plane A or B, P_j is the corresponding 3D–2D projection matrix, $\boldsymbol{M}(\boldsymbol{\varphi})_i$ is the ith point of the point cloud model for parameter set $\boldsymbol{\varphi}$, and the function $I_{N,j}(\cdot)$ denotes bilinear interpolation of an image at a specified 2D point on the detector. The last term of the cost function is a penalty term with weighting factor λ which increases the total cost for large parameter changes between $\boldsymbol{\varphi}$ and the initial guess $\boldsymbol{\varphi}_0$. In midsequence, the initial guess for a frame is the final result from the previous frame. Initialization of the first frame is described in Section 2.C.

The parameter optimization for the point cloud model is performed in three steps. The first step estimates only a global translation vector. In the second step, rotation and stent diameter are added to the set of adjustable parameters. The final step optimizes all model parameters. For the rigid registration in the first step, a weighting factor of $\lambda = 0$ is used. The two other steps use $\lambda = 1.0$. The cost function is minimized in each step of the optimization procedure using the Nelder–Mead method,[25] which for an N-dimensional function defines an (N + 1)-simplex, where N is the number of parameters (within this work $N = 10$). The algorithm then performs a series of reflection, expansion, contraction, and shrinkage steps to move the simplex toward the minimum of the cost function. In each step, the vertex of the simplex which represents the highest cost is selected and reflected through the centroid of the remaining vertices. If the new point has a lower cost than all remaining points, an expansion is performed to increase the step size. If the costs are higher than for all remaining points, a contraction is performed. Finally, if the reflected point is worse than the original point, a shrinkage step is performed, which replaces all points except the best to reduce the size of the simplex.

2.C. Initialization

In order to find a good initial approximation of the valve position and shape for the first frame, the proposed method detects corner points in the image according to Rublee et al.[30] Therefore, candidate pixels are first determined using the FAST algorithm.[26] FAST calculates the difference between the gray value of each pixel and the average value of the pixels along a circle with a fixed radius r_{FAST} around it. If the difference exceeds a threshold τ_{FAST}, then the pixel is considered a candidate. For this work, empirically determined parameters of $r_{\mathrm{FAST}} = 9$ pixels and $\tau_{\mathrm{FAST}} = 20$ pixels are used. The candidates are calculated for eight different pyramid levels and are then sorted using the Harris score,[31] which is a measure for the cornerness of a point. Only the 500 points with the highest score are analyzed further as described below. An example of the extracted corner points is shown in Fig. 5(a).

Due to the stent structure of the valve, a high number of salient corner points can usually be found at the device position in the image. A first estimate of the valve position is obtained by calculating the number of corner points within a small circular region around each pixel. The size of the region is set such that it is slightly larger than the size of the valve stent positioned at the isocenter and projected into the image plane. A radius of 70 pixels was used within this work. The centroid of the region with the most corner points is used as initial approximation as shown in Fig. 5(b). To exclude corner points which are not part of the valve, the position and orientation of a 50 × 110 pixel box are optimized by maximizing the number of corner points within this area. The size of the region is slightly larger than a prosthetic valve in its undeployed stage. All points outside of that region are excluded as shown in Fig. 5(c). Finally, the smallest rotated bounding box is determined for the remaining corner points by minimizing the area of the box as shown in Fig. 5(c). Given the centers $\boldsymbol{c}_A$ and $\boldsymbol{c}_B$ of the resulting bounding boxes in both image planes, the 3D position of the valve $\boldsymbol{c}_{3\mathrm{D}}$ can be calculated by backprojecting both points into the volume space and finding the closest point to both projection rays

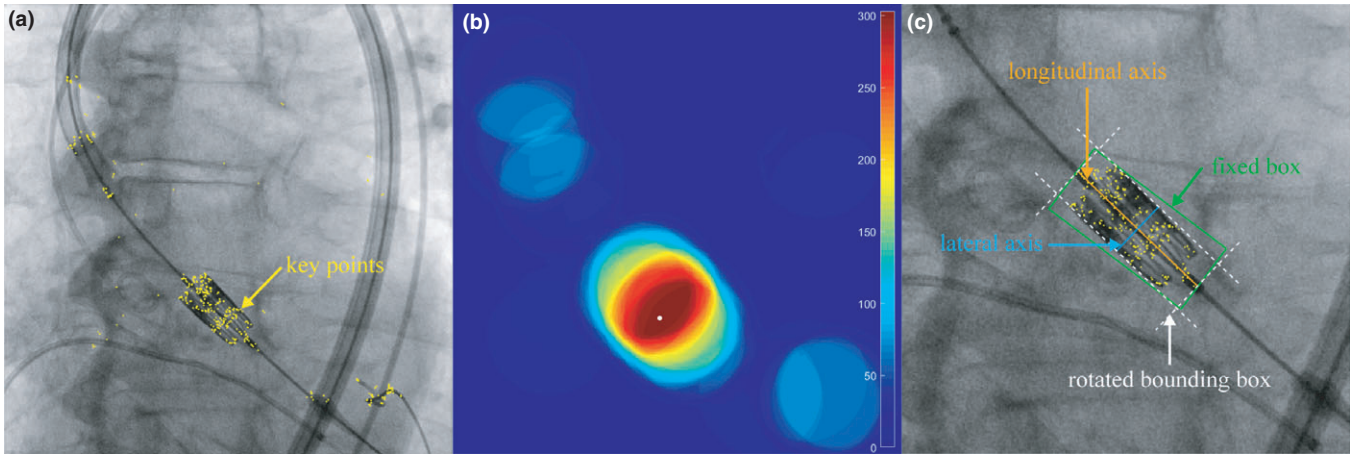

FIG. 5. Intermediate results of the initialization algorithm applied to a clinical dataset. (a) Selection of FAST key points based on the Harris score. (b) Number of corner points within 11 mm radius around each pixel with centroid of the maximum area shown as white circle. (c) Rotated box for corner point selection, rotated bounding box of remaining corner points, and lateral and longitudinal axes. [Color figure can be viewed at wileyonlinelibrary.com]

$$\boldsymbol{c}_{3D} = \frac{1}{2}(\boldsymbol{v}_A + \lambda_A \boldsymbol{b}_A + \boldsymbol{v}_B + \lambda_B \boldsymbol{b}_B), \tag{7}$$

with

$$\lambda_A = \frac{\left[(\boldsymbol{b}_A^\top \boldsymbol{b}_B)\boldsymbol{b}_B - \|\boldsymbol{b}_B\|\boldsymbol{b}_A\right]^\top (\boldsymbol{v}_A - \boldsymbol{v}_B)}{\|\boldsymbol{b}_A\|\|\boldsymbol{b}_B\| - (\boldsymbol{b}_A^\top \boldsymbol{b}_B)^2} \tag{8}$$

By switching $\boldsymbol{b}_A$ and $\boldsymbol{b}_B$, λ_B can be calculated in a similar manner. The variables $\boldsymbol{v}_A$ and $\boldsymbol{v}_B$ denote the focal spots of plane A and B, respectively, and $\boldsymbol{b}_A$ and $\boldsymbol{b}_B$ are the direction vectors pointing from $\boldsymbol{c}_A$ or $\boldsymbol{c}_B$ to the respective focal spot. An illustration of the projection geometry is shown in Fig. 6. The $\boldsymbol{b}$ vectors can be calculated using

$$\boldsymbol{b}_{A/B} = \boldsymbol{Q}_{A/B}\begin{pmatrix} \boldsymbol{c}_{A/B} \\ 1 \end{pmatrix}, \tag{9}$$

where $\boldsymbol{Q}_{A/B}$ is the inverse of the upper left 3×3 submatrix of the projection matrix of plane A or B. The 3D orientation of the valve is determined by backprojecting the longitudinal axes $\boldsymbol{l}_A$ and $\boldsymbol{l}_B$ of the 2D bounding boxes into the 3D volume space. The intersection of the resulting two planes defines the longitudinal axis $\boldsymbol{l}_{3D}$ of the valve in 3D.

$$\boldsymbol{l}_{3D} = \left[\boldsymbol{Q}_A\begin{pmatrix} \boldsymbol{l}_A \\ 0 \end{pmatrix} \otimes \boldsymbol{b}_A\right] \otimes \left[\boldsymbol{Q}_B\begin{pmatrix} \boldsymbol{l}_B \\ 0 \end{pmatrix} \otimes \boldsymbol{b}_B\right] \tag{10}$$

Finally, the diameter $\boldsymbol{d}_{3D}$ of the valve is calculated by backprojecting the lateral axis of the bounding boxes $\boldsymbol{u}_A$ and $\boldsymbol{u}_B$.

$$d_{3D} = \frac{1}{2}(\|\boldsymbol{Q}_A \boldsymbol{u}_A\| + \|\boldsymbol{Q}_B \boldsymbol{u}_B\|) \tag{11}$$

2.D. Simulated image data

The proposed algorithm was evaluated using simulated as well as real fluoroscopic image sequences. The simulation was based on the 4D digital XCAT phantom,[32] which simulates realistic human anatomy and includes sophisticated respiratory and cardiac motion models. For each time frame, a

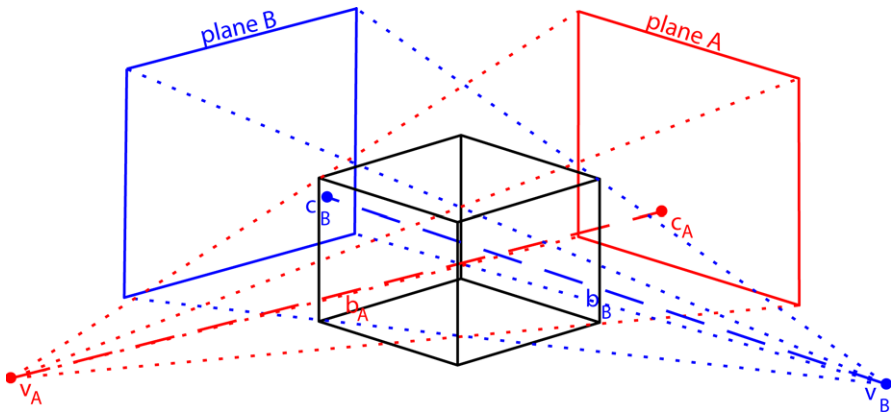

FIG. 6. Illustration of the projection geometry. The vectors v, b, and c are used in the initialization algorithm. [Color figure can be viewed at wileyonlinelibrary.com]

voxelized version of the XCAT phantom was created with an isotropic resolution of 0.2 mm. The valve model was placed in the cardiac region of the XCAT phantom. Ten biplane projection sequences with 150 frames were created using a respiratory cycle time of 5 s, a heart rate of 60 bpm, and a frame rate of 15 fps. The virtual projection angles were set to −90° (lateral) and 0° (anterior–posterior). An orthogonal projection geometry was used for the simulations, where the projection images were determined by the line integrals along the y- and x-dimensions, respectively. The valve diameter vs time was described with a smooth monotonically increasing function, the change in slant over time was modeled by a piecewise linear function, and the upper and lower flare angles were allowed to continuously increase during the expansion.

An example of the simulated valve shape parameters can be found in Fig. 7. The translation and rotation of the valve consisted of three components. Respiratory and cardiac induced motion components were synchronized with the respiratory and cardiac motion of the XCAT phantom. Superimposed on the cardiorespiratory motion was a general motion component representing the operator movements to adjust the device position. The motion parameters were randomized to create different paths and expansion evolutions in each sequence.

The size of the simulated projection images was 512 × 512 pixels corresponding to a 102.4 × 102.4 mm field of view. Additionally, different amounts of Poisson noise were added to the projection images to create realistic fluoroscopy or cine quality images. Image sequences with a contrast to noise ratio (CNR) of 3, 6, and 15 and no noise were created. For comparison, the CNR was measured in real fluoroscopic and cine images of the valve in a water bath. The signal difference between the device and the surrounding water divided by the standard deviation of the noise was 6 and 15, respectively.

2.E. Experimental image data

For the real fluoroscopic acquisitions, a SAPIEN XT 26 mm valve was placed inside a cylindrical plastic container filled with water. The valve was mounted on a balloon catheter, which was guided through a hole in the lid of the container as shown in Fig. 8. This allowed for changes to the position, orientation, and expansion state of the valve without opening the container. Using a biplane angiography system (Artis Zee, Siemens, Forchheim, Germany), a rotational 3D acquisition with 496 projection images over a range of 210° was performed. The valve was then slightly expanded using the balloon catheter, and the position and orientation were modified. Afterward, another rotational acquisition was performed. This process was repeated until the valve was completely expanded, resulting in 16 acquisitions. Additionally, a rotational acquisition of a chest phantom with embedded ribcage and spine (see Fig. 8) was performed. All images were converted into line integral images using software provided by the manufacturer of the imaging system. In order to add realistic anatomical background to the images of the valve, the empty cylindrical container was subtracted from the line integral images of the valve acquisitions and the chest

FIG. 8. Experimental setup for C-arm CT acquisitions. Left: Sapien XT 26 mm valve is mounted on an inflatable balloon catheter within a water-filled cylindrical container. The catheter is guided through a sealed hole in the lid of the container. Right: Chest phantom used for anatomical background. [Color figure can be viewed at wileyonlinelibrary.com]

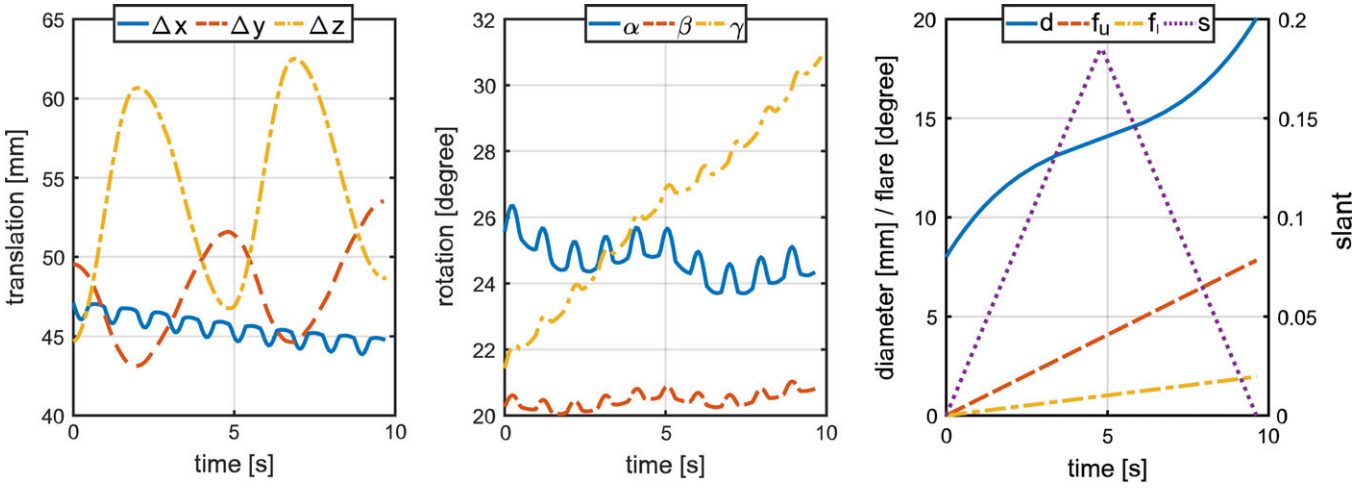

FIG. 7. Example of ground truth valve parameters for simulated valve motion and expansion. Translation (left) and rotation (center) vectors parameters consist of cardiac and respiratory component as well as a random low-frequency component. The upper and lower flare angles f_u and f_l are represented by a linear function. The slant s is described by a piecewise linear function, where the total range of values is in the interval from −1 to 1. The valve diameter d monotonically increases during the simulated expansion. [Color figure can be viewed at wileyonlinelibrary.com]

phantom images were added to the result. Dynamic image sequences were then created by extracting the images for one projection angle from each acquisition. Biplane image sequences were created for gantry positions of −90° and 0° as well as −45° and 45°. Poisson noise was added to generate images with a signal-to-noise ratio similar to standard fluoroscopy images.

With this experimental design, the volumetric CT reconstruction generated from a rotational scan provides the ground truth reference for the valve position, orientation, and shape, at a particular state of valve expansion. The 3D reconstruction obtained from two projections of a rotation is directly compared to the CT image from the same rotation. The CT images were reconstructed with an isometric voxel size of 0.14 mm and a volume size of 512 × 512 × 387 voxels.

2.F. Evaluation

The target registration error (TRE) was used to quantify the accuracy of the 3D valve representation. The TRE was calculated for nine corner points on the upper and lower ends of the valve as shown in Fig. 9. The true positions of these points are inherently known for the simulated data. For the experimental data, the true positions were extracted from the voxelized reconstructions. First, the valve was segmented from the cone-beam CT volume using global intensity thresholding. A cylinder was then fitted to the segmented object to estimate the longitudinal axis of the valve. All points within a 0.7 mm thick slice at the upper and lower end of the valve were then grouped into nine clusters using the k-means algorithm. The centroid of each group was then used as corner point in the CT volume. The TRE was calculated as the root-mean-squared error between the estimated valve corner points $\widehat{\boldsymbol{p}}_i$ obtained from biplane imaging and the true corner points $\boldsymbol{p}_i$ obtained from CT,

$$\mathrm{TRE} = \sqrt{\frac{1}{n}\sum_{i=1}^{n} \|\boldsymbol{p}_i - \widehat{\boldsymbol{p}}_i\|^2} \tag{12}$$

where $n = 18$ is the number of corner points. Additionally, the accuracies of the orientation of the longitudinal axis, the centroid location, and the valve diameter were evaluated.

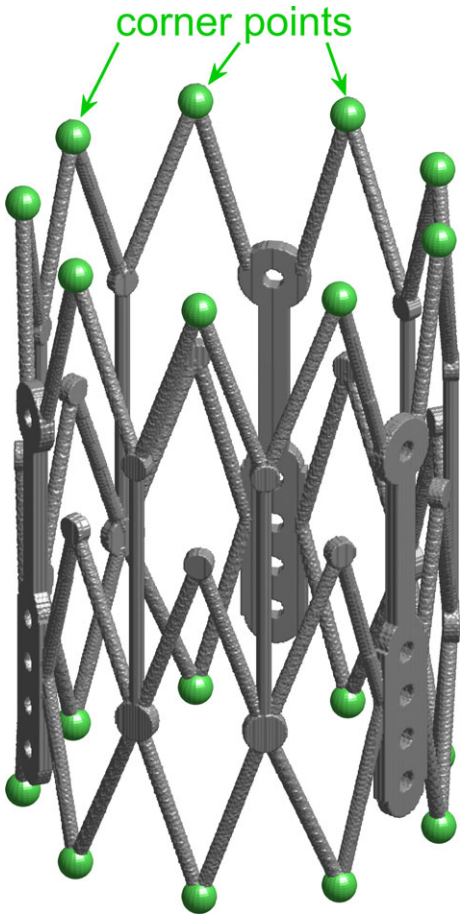

FIG. 9. Points of interest for the calculation of the target registration error (TRE). [Color figure can be viewed at wileyonlinelibrary.com]

3. RESULTS

To enable successful tracking of the valve using biplane fluoroscopic image sequences, a good estimate of the position, orientation, and diameter of the valve is necessary. The proposed initialization technique was able to locate the valve in the initial frames of the image sequences with a TRE of 0.72 ± 0.24 mm in the simulated images and 0.73 ± 0.19 mm in the phantom experiments. The initial orientation of the 3D longitudinal axis was determined with an error of 1.24° ± 1.74° in simulation and 1.40° ± 0.98° in experiment. The diameter errors were 0.21 ± 0.11 mm and 0.10 ± 0.07 mm, respectively. Figure 10 shows a detailed

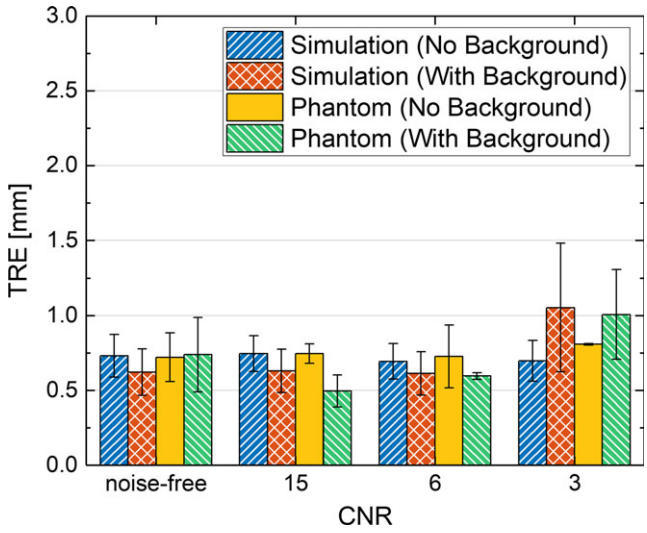

FIG. 10. Performance of initialization based on the first frame of a fluoroscopic image sequence, expressed as the average and standard deviation of the target registration error (TRE) in millimeter. Results are shown for simulations and phantom experiments, with and without anatomical background, and different image contrast to noise ratios (CNR). [Color figure can be viewed at wileyonlinelibrary.com]

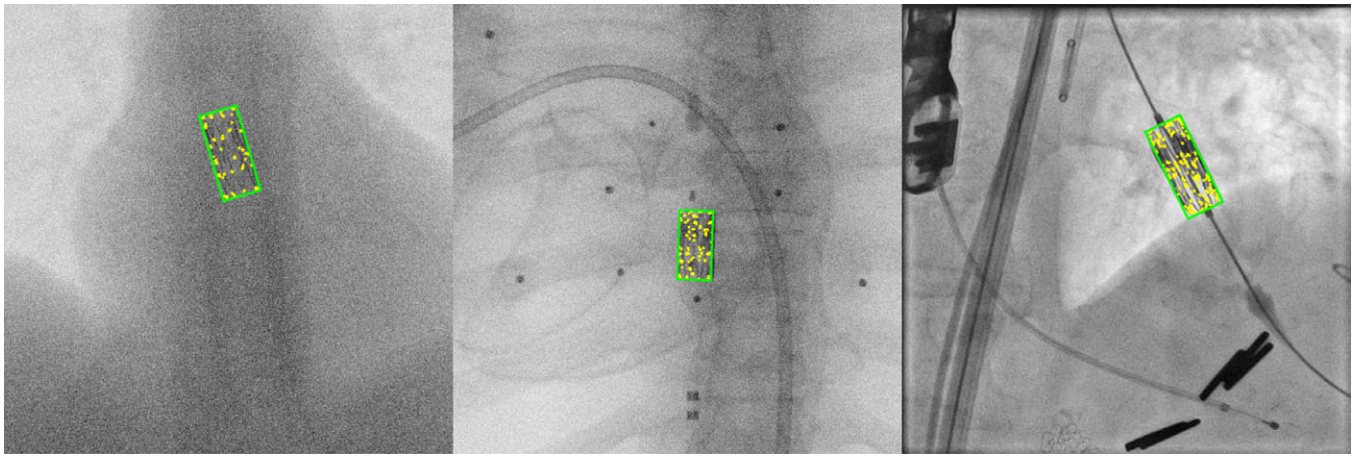

FIG. 11. Examples of the 2D initialization results. Left image shows a result from the simulation with CNR = 3. The center image is from the phantom experiment (CNR = 3), where a chest phantom, fiducials, and a guiding sheath provided background. The image on the right shows the initialization results for a clinical image from an actual TAVR procedure. A TEE probe appears in the upper left corner. [Color figure can be viewed at wileyonlinelibrary.com]

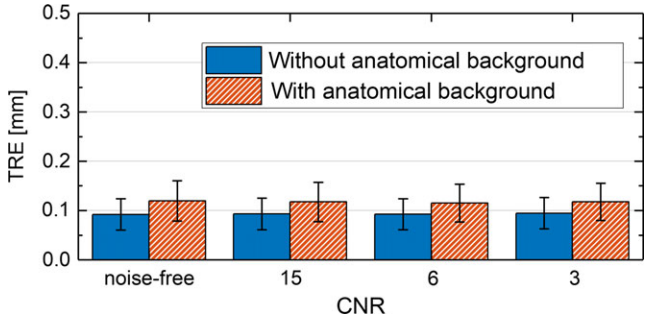

FIG. 12. Average target registration error (TRE) in millimeter for the simulated fluoroscopic sequences with different contrast to noise ratio. The error bars indicate the standard deviation of the TRE. The results are shown with and without anatomical background added using the XCAT phantom. [Color figure can be viewed at wileyonlinelibrary.com]

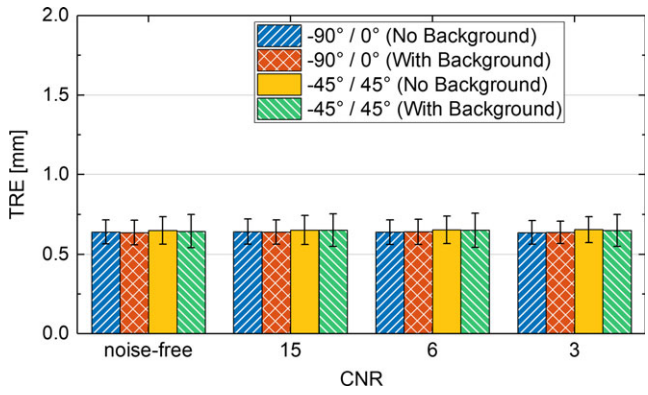

FIG. 13. Comparison of the target registration error (in mm) results for the phantom experiments at different gantry angles and noise levels, with and without anatomical background. The error bars represent the standard deviation of the TRE. Gantry angles are AP-lateral (-90° / 0°) and (-45°/45°). [Color figure can be viewed at wileyonlinelibrary.com]

analysis of the initialization TRE for the simulated and phantom experiments, with and without anatomical background. Examples of the initialization results for the simulated and phantom images are shown in Fig. 11. The initialization technique was also applied to a clinical image of a TAVR procedure (Fig. 11, right); however, since no ground truth is available, only a visual comparison is provided. The experimental and clinical images contain additional high contrast objects such as fiducials and an ultrasound probe.

Using these initialization results, the position, orientation, and shape of the valve were tracked for each frame of the image sequences. The average and standard deviation of the target registration error for the simulated fluoroscopic image sequences are shown in Fig. 12. The simulation without anatomical background yielded an average TRE of less than 0.1 mm for all noise levels. Using the XCAT phantom, the average TRE slightly increased to 0.12 ± 0.04 mm. The average location error of the valve measured at the center of mass was 0.03 ± 0.02 mm. The error in the estimated orientation of the longitudinal axis was $0.20^\circ \pm 0.11^\circ$ and the error in the estimated diameter was 0.03 ± 0.02 mm.

The tracking results of the phantom experiments are shown in Fig. 13. The tracking algorithm yielded TRE results for image sequences with and without anatomical background of 0.64 ± 0.09 mm and 0.65 ± 0.08 mm, respectively. The location error of the valve measured at the center of mass was 0.52 ± 0.08 mm. The error in the estimated orientation of the longitudinal axis was $0.72^\circ \pm 0.45^\circ$ and the error in the estimated diameter was 0.12 ± 0.07 mm. Examples of the tracking results in 2D and 3D are shown in Fig. 14.

The symmetry of the real valve in an expanded state was also evaluated to validate the assumptions of a symmetrically expanding model with rigid parts. Therefore, a CT volume of the expanded valve was analyzed by extracting the corner points at the lower end of the valve. The angles between the elements were then measured and compared to the mathematical model at the same expansion state. Figure 15 shows the direct comparison between the real expanded valve and the model. In both the model and real valve, the angles between corner points that enclose an SVC component are slightly

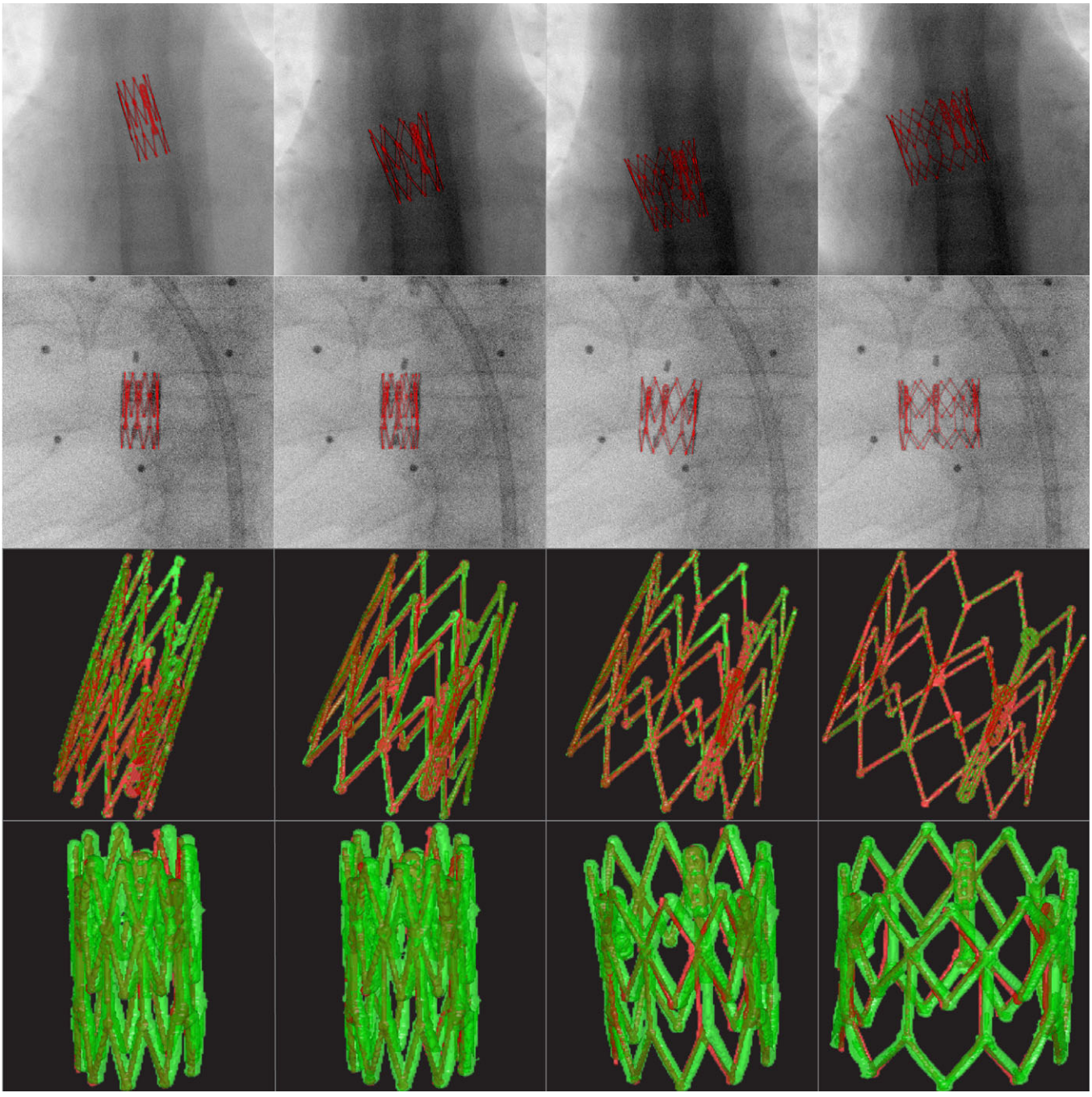

FIG. 14. Example images of prosthetic valve tracking. The top row shows an overlay of the forward projected valve model on the simulated x-ray images from one plane of the biplane system, at four states of valve expansion. The second row shows a similar overlay result from the experimental study. The third and fourth rows show the correspondence between the 3D valve model determined from biplane imaging and the ground truth or reference. Results of the simulation are shown in row 3, while the results from the experimental study are shown in row 4. [Color figure can be viewed at wileyonlinelibrary.com]

larger ($\sim 2°$) than the angles between regular corner points that do not enclose an SVC component. In the CT acquisition of the real valve, the standard deviation of the regular angles was 1.38°, and the standard deviation of the angles enclosing an SVC component was 0.47°.

4. DISCUSSION

The presented technique for motion and deformation tracking of prosthetic valves in biplane fluoroscopic images shows consistent results with submillimeter accuracy. The initialization approach based on corner points was able to find the outline of the valve in all image sequences, which allowed the initialization of position, orientation, and diameter of the 3D model. In the phantom experiments, comparable initialization results were achieved for sequences with and without anatomical background despite the presence of high contrast fiducials. Also, in a clinical image containing a transesophageal echo probe and other high contrast devices which may generate a considerable number of corner points, the

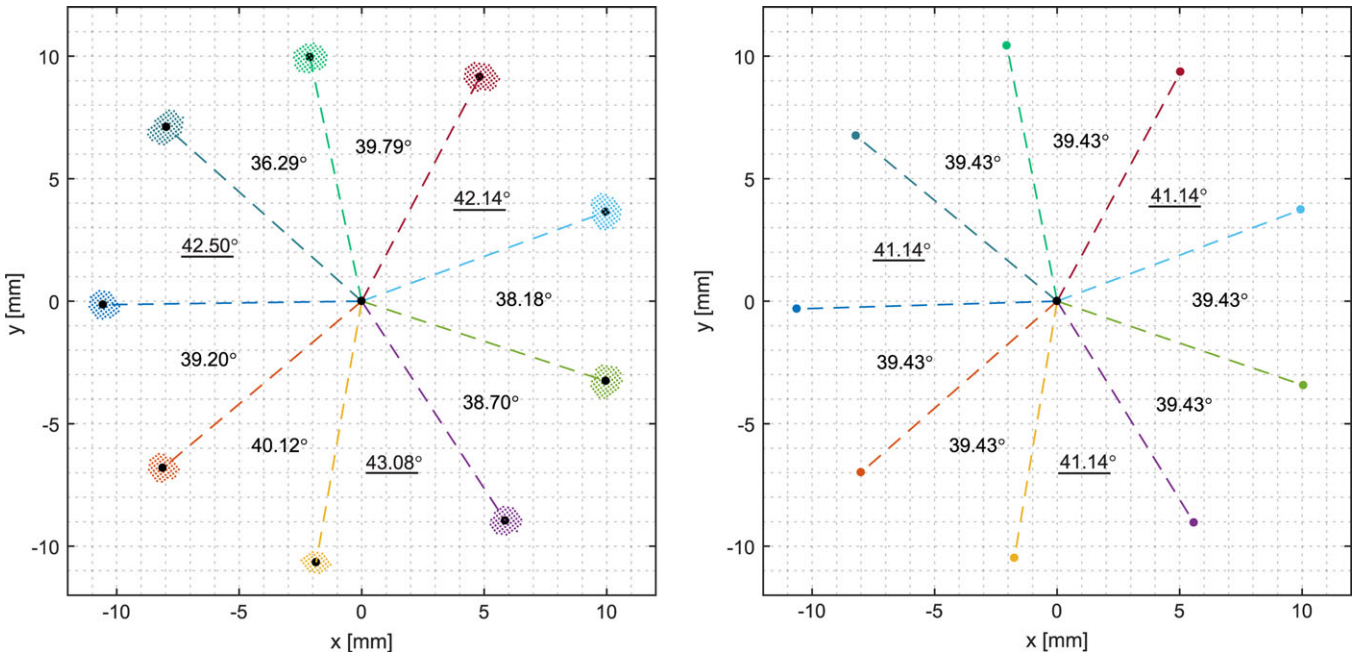

FIG. 15. Symmetry evaluation of the real prosthetic valve (left) compared to the model (right). Points around the center denote the corner points used for TRE calculation at the lower part of the valve. The angles shown underlined are slightly larger due to the SVC components. [Color figure can be viewed at wileyonlinelibrary.com]

valve was correctly identified. However, it should be mentioned that some other configurations of high contrast objects might cause the algorithm to fail or to deliver inaccurate results. For a clinical application, this could be resolved by a manual interaction of the user in cases where the automatic initialization fails.

The model-based tracking algorithm was able to determine the position, orientation, and shape of the valve in 3D reliably. The tracking accuracy can be influenced by the image quality, the gantry angles, or anatomical features in the background of the valve. However, as demonstrated in Figs. 12 and 13, similar results were achieved across all noise levels tested as well as for the different gantry positions and no considerable differences were observed between the groups. The accuracy achieved in the simulated image sequences is considerably better than in the phantom experiments. This is expected, since the device model used to generate image data was of the same general form as that used in tracking. However, the phantom experiments demonstrate that tracking can still be performed even when the device model is not perfectly matched to the real device. For example, the valve model in this study assumed symmetrical expansion of the valve and rigid elements of the stent structure. Deviations from this ideal expansion behavior can cause small mismatches between the final model and ground truth. However, in experiments, the device representations were still obtained with a TRE of 0.62 mm. This is comparable to about 3/4 of the diameter of the vertical and diagonal struts.

Anatomical structures in the image background only slightly affected the accuracy in the simulated images. In the phantom experiments, the aforementioned effects of valve asymmetry outweigh the influence of other structures in the background. In a clinical application, the interaction of the valve with anatomical structures might cause additional variation in the valve symmetry. However, Willson et al.[33] determined that balloon-expandable stents such as the one used within this work maintained 96% circularity in 48 of 50 cases in an analysis of TAVR patients 1-yr postprocedure.

The proposed technique can be used with other types of prosthetic valves with stent-like support structures. However, a separate model is required for each valve type. The behavior of a valve type can be characterized by high-resolution CT scanning of the valve at different states of expansion. However, at this point, there is no automated method to generate the dynamic point cloud model. Instead, it requires careful analysis of the stent deformations that occur during expansion. The degrees of freedom in valve shape can vary for different valve types.

A real-time implementation of the proposed algorithm might help the physician to better appreciate the valve apposition within the annulus and to predict potential problems such as paravalvular leak, risk of embolization, and coronary obstruction. For repositionable valves, it might also help the operator to find the optimal valve position. The data collected during a procedure might also help in the development and engineering of future valves with the aim of minimizing complications.

5. CONCLUSION

The proposed technique shows a novel approach which enables tracking of the position, orientation, and shape of prosthetic heart valves in 3D, based on biplane fluoroscopy and a mathematical model of the valve. The results shown

here demonstrate that submillimeter accuracy is possible. The results could be used to combine a 3D valve representation with live 3D echocardiography acquisitions of the soft-tissue structures of the heart. Such an approach to the visualization of device and anatomy may help the physician better appreciate valve placement during a procedure and possibly allow for improved prediction of potential problems.

ACKNOWLEDGMENTS

Funding was received from Siemens Healthineers. The concepts presented in this paper are based on research and are not commercially available.

CONFLICTS OF INTEREST

Dr. Hatt and Dr. Speidel have a patent on the subject matter described in this work.

[a]Author to whom correspondence should be addressed. Electronic mail: speidel@wisc.edu

REFERENCES

1. Holmes DR, Nishimura RA, Grover FL, et al. Annual outcomes with transcatheter valve therapy. *J Am Coll Cardiol*. 2015;66:2813–2823.
2. Gao G, Penney G, Ma Y, et al. Registration of 3D trans-esophageal echocardiography to X-ray fluoroscopy using image-based probe tracking. *Med Image Anal*. 2012;16:38–49.
3. Housden RJ, Arujuna A, Ma Y, et al. Evaluation of a real-time hybrid three-dimensional echo and X-ray imaging system for guidance of cardiac catheterisation procedures. In: *International Conference on Medical Image Computing and Computer-Assisted Intervention*. Berlin: Springer; 2012:25–32.
4. Hatt CR, Speidel MA, Raval AN. Real-time pose estimation of devices from x-ray images: application to x-ray/echo registration for cardiac interventions. *Med Image Anal*. 2016;34:101–108.
5. Lang P, Seslija P, Chu MW, et al. US-fluoroscopy registration for transcatheter aortic valve implantation. *IEEE Trans Biomed Eng*. 2012;59:1444–1453.
6. Faletra FF, Pedrazzini G, Pasotti E, Murzilli R, Leo LA, Moccetti T. Echocardiography–X-ray image fusion. *JACC Cardiovasc Imaging*. 2016;9:1114–1117.
7. Brost A, Strobel N, Yatziv L, et al. Geometric accuracy of 3-D X-ray image-based localization from two C-arm views. In: Workshop on Geometric Accuracy in Image Guided Interventions-Medical Image Computing and Computer Assisted Interventions, MICCAI; 2009:12–19.
8. Wagner M, Schafer S, Strother C, Mistretta C. 4D interventional device reconstruction from biplane fluoroscopy. *Med Phys*. 2016;43:1324–1334.
9. Baert SAM, van de Kraats EB, van Walsum T, Viergever MA, Niessen WJ. Three-dimensional guide-wire reconstruction from biplane image sequences for integrated display in 3-D vasculature. *IEEE Trans Med Imaging*. 2003;22:1252–1258.
10. Hoffmann M, Brost A, Jakob C, et al. Reconstruction method for curvilinear structures from two views. In: *Proc. SPIE 8671, Medical Imaging 2013: Image-Guided Procedures, Robotic Interventions, and Modeling*. Vol. 8671; 2013:86712F–86712F-8.
11. Wahle A, Oswald H, Fleck E. 3D heart-vessel reconstruction from biplane angiograms. *IEEE Comput Graph Appl*. 1996;16:65–73.
12. Schenderlein M, Stierlin S, Manzke R, Rasche V, Dietmayer K. Catheter tracking in asynchronous biplane fluoroscopy images by 3D B-snakes; 2010:76251U.
13. Uneri A, Goerres J, De Silva T, et al. Deformable 3D–2D registration of known components for image guidance in spine surgery. In: *Medical Image Computing and Computer-Assisted Intervention – MICCAI 2016*. Cham, Switzerland: Springer International Publishing AG; 2016:124–132.
14. Haase C, Schäfer D, Dössel O, Grass M. 3D ablation catheter localisation using individual C-arm x-ray projections. *Phys Med Biol*. 2014;59:6959–6977.
15. Haase C, Schäfer D, Dössel O, Grass M. Model based 3D CS-catheter tracking from 2D X-ray projections: binary versus attenuation models. *Comput Med Imaging Graph*. 2014;38:224–231.
16. Radeva P, Toledo R, Land CV, Villanueva J. 3D vessel reconstruction from biplane angiograms using snakes. In: *Computers in Cardiology 1998. Vol. 25 (Cat. No.98CH36292)*; 1998:773–776.
17. Canero C, Vilarino F, Mauri J, Radeva P. Predictive (un)distortion model and 3-D reconstruction by biplane snakes. *IEEE Trans Med Imaging*. 2002;21:1188–1201.
18. Prause GPM, Onnasch DGW. Binary reconstruction of the heart chambers from biplane angiographic image sequences. *IEEE Trans Med Imaging*. 1996;15:532–546.
19. Lamecker H, Wenckebach TH, Hege HC. Atlas-based 3D-shape reconstruction from X-ray images. In: *18th International Conference on Pattern Recognition (ICPR'06)*. Vol. 1; 2006:371–374.
20. Baka N, Kaptein BL, de Bruijne M, et al. 2D–3D shape reconstruction of the distal femur from stereo X-ray imaging using statistical shape models. *Med Image Anal*. 2011;15:840–850.
21. Kurazume R, Nakamura K, Okada T, et al. 3D reconstruction of a femoral shape using a parametric model and two 2D fluoroscopic images. *Comput Vis Image Underst*. 2009;113:202–211.
22. Zheng G, Schumann S. 3D reconstruction of a patient-specific surface model of the proximal femur from calibrated x-ray radiographs: a validation studya). *Med Phys*. 2009;36:1155–1166.
23. Zheng G, Ballester MÁG, Styner M, Nolte L-P. Reconstruction of patient-specific 3D bone surface from 2D calibrated fluoroscopic images and point distribution model. In: *Medical Image Computing and Computer-Assisted Intervention – MICCAI 2006*. Heidelberg, Germany: Springer-Verlag; 2006:25–32.
24. Hatt CR, Wagner M, Raval AN, Speidel MA. Dynamic tracking of prosthetic valve motion and deformation from bi-plane x-ray views: feasibility study. Vol. 9786; 2016:978604–978604-10.
25. Nelder JA, Mead R. A simplex method for function minimization. *Comput J*. 1965;7:308–313.
26. Rosten E, Drummond T. Machine learning for high-speed corner detection. In: *Comput Vision–ECCV 2006*. Heidelberg, Germany: Springer-Verlag; 2006:430–443.
27. Yang K, Kwan ALC, Miller DF, Boone JM. A geometric calibration method for cone beam CT systems. *Med Phys*. 2006;33:1695–1706.
28. Fahrig R, Holdsworth DW. Three-dimensional computed tomographic reconstruction using a C-arm mounted XRII: image-based correction of gantry motion nonidealities. *Med Phys*. 2000;27:30–38.
29. Jaffray DA, Siewerdsen JH, Wong JW, Martinez AA. Flat-panel cone-beam computed tomography for image-guided radiation therapy. *Int J Radiat Oncol*. 2002;53:1337–1349.
30. Rublee E, Rabaud V, Konolige K, Bradski G. ORB: an efficient alternative to SIFT or SURF. In: *2011 International conference on computer vision*; 2011:2564–2571.
31. Harris C, Stephens M. A combined corner and edge detector; 1988:23.1–23.6.
32. Segars WP, Sturgeon G, Mendonca S, Grimes J, Tsui BMW. 4D XCAT phantom for multimodality imaging research. *Med Phys*. 2010;37:4902–4915.
33. Willson AB, Webb JG, Gurvitch R, et al. Structural integrity of balloon-expandable stents after transcatheter aortic valve replacement: assessment by multidetector computed tomography. *JACC Cardiovasc Interv*. 2012;5:525–532.